Automated analysis of spectroscopic data for cQED systems

G.Fedorov[1, 2, a)] and A. Ustinov[1, 3]
[1)]*Russian Quantum Center, Skolkovo village, Russia*
[2)]*Moscow Institute of Physics and Technology, Dolgoprundiy, Russia*
[3)]*Karlsruhe Institute of Technology, Karlsruhe, Germany*

(Dated: 12 December 2018)

To build a full-scale quantum processor it is necessary to automate as many steps as possible on the physical, hardware level. Circuit quantum electrodynamics (cQED) is a contemporary architecture for dispersive readout and Purcell protection of superconducting qubits of various types, and thus it is necessary to develop software that is able to perform every kind of automatic calibration of such systems from scratch without any human participation. An important step towards this goal is to build a noise-insensitive and accurate computer vision tool to process three-dimensional spectroscopic data. In this work, we present and describe two scalable algorithms that are able to extract the Hamiltonian parameters of the cQED systems from spectroscopic data.

I. INTRODUCTION

Computation on a quantum computer involves operating large numbers of physical quantum bits (qubits). One of the most significant challenges is that today's qubit systems are not produced identical and cannot be operated identically[1,2]: typically, control parameters for a device are determined by following a sequence of calibration experiments, and vary among the devices. Since manual tuning of these parameters is not a scalable solution, operating a few dozens of qubits requires developing an autonomous system able to handle the physical device calibration on its own. Moreover, a lot of research is still being done to find the optimal chip designs and fabrication methods. This research includes gathering statistics on many different samples that should be measured and consistently evaluated. An automated tool not only will speed up this process, but as well exclude human error.

In this work, we are proposing and implementing several methods of data processing and computer vision that aid automatic calibration of circuit QED[3] architectures used to read out superconducting qubits' states. Computer vision is understood here as an enterprise that uses statistical methods to disentangle data using models constructed with the aid of geometry, physics, and learning theory[4]. As it will be shown below the output of circuit calibration is almost always an image and it is hardly possible to automatically extract the required information from it without resorting to methods of computer vision.

The proposed methods are accurate, fast and robust to noise, applicable to superconducting qubits with a periodic and parametrizable spectrum, and compatible with the state-of-the-art paradigm of one readout resonator per one qubit[5,6]. Therefore, the suggested approach is scalable and can be applied to processors with any number of qubits.

The flow of an experiment that characterizes a single qubit on a chip is depicted schematically in Fig. 1(a). It is similar to the classic procedures described in Refs. [2 and 7] for measuring cQED samples with qubits of tunable frequency. For non-tunable qubits, a different algorithm of automatic calibration is described in the patent application Ref. [8].

First of all, it is necessary to detect the positions of the resonance peaks corresponding to the readout resonators. Resonator search provides the scan range for the probe frequency Δf_p in single-tone spectroscopy (STS). STS records the behaviour of the resonance peak while changing the magnetic field applied to the sample (controlled by some current I). By processing the results of the STS, one can estimate the qubit frequency depending on I (this coarse estimation is denoted as $f_{ge}^{(0)}(I)$). Conversely, the resonator frequency $f_r(I)$ and the coupling strength g may be found accurately. Based on these results, one may set the scan range for the two-tone spectroscopy (TTS) in excitation frequency Δf_{exc} and current ΔI. Next, from TTS, we can obtain various qubit transition frequencies dependence on current $f_{ge}(I), f_{gf/2}(I)$, etc. with accuracy sufficient for pulsed experiments. After that, pulsed calibrations may be started to optimize gate fidelities. In overall, the process is structured so that the results of one measurement define the parameters of the next, successively acquiring more accurate information about the physical system.

The measurement outcomes that contain information about the system properties may be divided in two groups: some results contain 1D curves (single-valued functions f(x)), and others contain 2D data (heatmap images, f(x,y)). The scope of this work is confined to the automatic analysis the latter results. In Fig. 1(b,c) we illustrate examples of correlated measured data and the theoretical model. Fig. 1(b) shows that STS data should be interpreted using two discontinuous curves (upper row) or a single continuous curve (lower row) that are defined by the model. Then, Fig. 1(c) shows how qubit spectral lines should be detected. The main problems here are that, firstly, several spectral lines may be observed even for a single qubit (and thus the model is not single-valued), secondly, that spurious non-qubit transitions should be ignored, and, finally, the noise.

The implementation of our methods relies on the theoretical description of the cQED systems and physical qubits; therefore, in Appendices A and B we derive all the necessary equations to form the model curves that are expected to appear in single- and two-tone spectroscopy. Without loss if generality,

[a)]Electronic mail: gleb.fedorov@phystech.edu

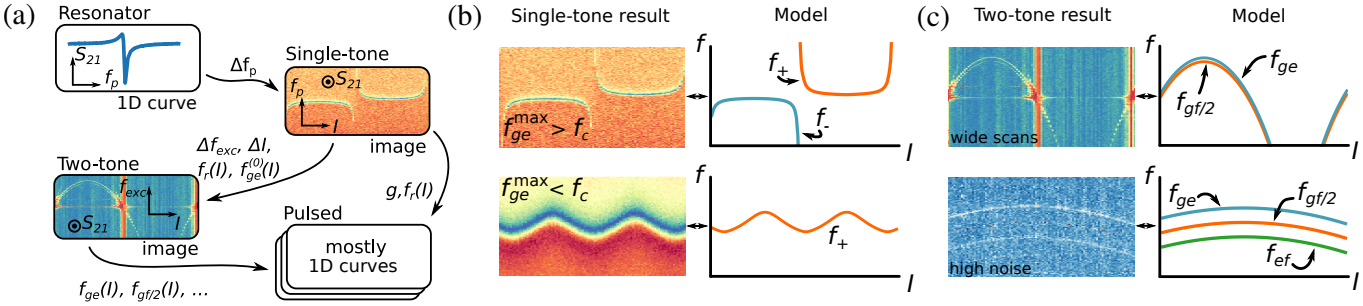

FIG. 1. (a) Common experiment flow for a tunable-frequency qubit: usually, three continuous wave spectroscopic measurements are performed before pulsed experiments, and each next experiment is based on the results of the previous ones. (b) Examples of the desired results after the detection for two qualitatively different STS outcomes. The heatmaps should be brought into correspondence with the 2D model curves. In the first row, two model curves that should be fitted simultaneously since the model is discontinuous. (c) Examples of the desired results after processing TTS data. The heatmap should be brought into correspondence with the model of the qubit spectrum which may not be single-valued since several transitions may be visible.

we use the transmon[9] with an asymmetric SQUID as a qubit; however, since our methods do not depend on the particular shape of the qubit transitions, for other types of qubits the logic will stay the same and there is no loss of generality.

For the singe-tone spectroscopy, they model curves are (see Fig. 1(b)):

$$f_{\pm}(I) \equiv f_r(I) = \frac{f_c + f_{ge}(I)}{2} \pm \sqrt{g^2 + (f_{ge}(I) - f_c)^2/4}, \quad (1)$$

where f_c stands for current-independent bare cavity frequency. Here we note that for the avoided crossings pattern both curves are necessary; alternatively, for the cases when the qubit is entirely below (above) the bare cavity frequency only $f_+(I)$ $(f_-(I))$ is used.

For the two-tone spectroscopy, we take the dependence of the qubit transitions on current $f_{ge,gf/2,ef}(I)$ are expressed as

$$f_{ge}(I) = f_{ge}^{max}\left[\cos^2\left(\frac{\pi(I-I_{ss})}{\Pi}\right) + d^2\sin^2\left(\frac{\pi(I-I_{ss})}{\Pi}\right)\right]^{\frac{1}{4}},$$
$$f_{gf/2} = f_{ge} + \alpha/2,\ f_{ef} = f_{ge} + \alpha \quad (2)$$

where Φ_0 is the flux quantum, d is the SQUID asymmetry, α is the anharmonicity of the transmon equal to it's negative charging energy $-E_C$, and f_{ge}^{max} is the qubit frequency at $I = I_{ss}$. I_{ss} (sweet spot current) is the current exactly compensating the non-zero residual flux that is always present in experiment coming from the local magnetic fields on the chip. Finally, Π is the period of the spectrum in current.

In overall, we have 6 fitting parameters for the single-tone (f_c, g, Π, I_{ss}, f_{ge}^{max}, d) and 5 parameters for the two-tone spectroscopy (Π, I_{ss}, f_{ge}^{max}, d, α).

The structure of the rest of the paper is as follows. First, we will describe our methods to process STS data and to detect qubit spectral lines on TTS data. Next, the accuracy, performance and reliability of both algorithms will be addressed. Finally, we discuss the limitations, possible applications and future work.

II. METHODS

In this section, we describe the approaches towards extraction of Hamiltonian parameters from the two types of spectroscopic measurement results. Additionally, we describe important peculiarities of the data itself and some essential experimental details.

A. Single-tone spectroscopy recognition

Usually, in the experiment the spectrum of the readout resonator is recorded using a vector network analyzer (VNA). The VNA measures a complex scattering parameter S_{ij} for a range of probe frequencies Δf_p around the resonance. Hence, one VNA scan may be represented as two 1D plots for the amplitude $|S_{ij}(f_p)|$ and the phase $\angle S_{ij}(f_p)$ of the scattering parameter. When the magnetic flux sweep is added, the data becomes three-dimensional and has to be represented visually using two heatmap plots for $|S_{ij}(f_p, I)|$ and $\angle S_{ij}(f_p, I)$. In Fig. 2(a) one can find an experimental heatmap from our database for a notch-type (side-coupled) coplanar waveguide resonator coupled to a tunable transmon qubit. Only the amplitude $|S_{21}(f_p, I)|$ is shown.

To extract the Hamiltonian parameters, we propose to fit the model (1) to the data in Fig. 2(a) in the sense of maximum likelihood. However, as one can see, the data are much more complex than the model as it contain an extra dimension. Even after the dimensionality reduction procedure (described below), the fitting is not a trivial task because the maximum likelihood estimation implicates global optimization. The situation is even more complicated since the we need to solve an optimization problem with an ill-defined loss function (i.e. in the least squares algorithm). This is so, firstly, due to the periodic dependence of the frequencies on current I and the unknown position of the qubit sweet spot I_{ss} and, secondly, due to the strongly non-linear dependence of the model on other parameters. Fortunately, it is possible to get a good initial guess for Π and I_{ss} parameters and then brute force the solution in other variables since we have well defined bounds

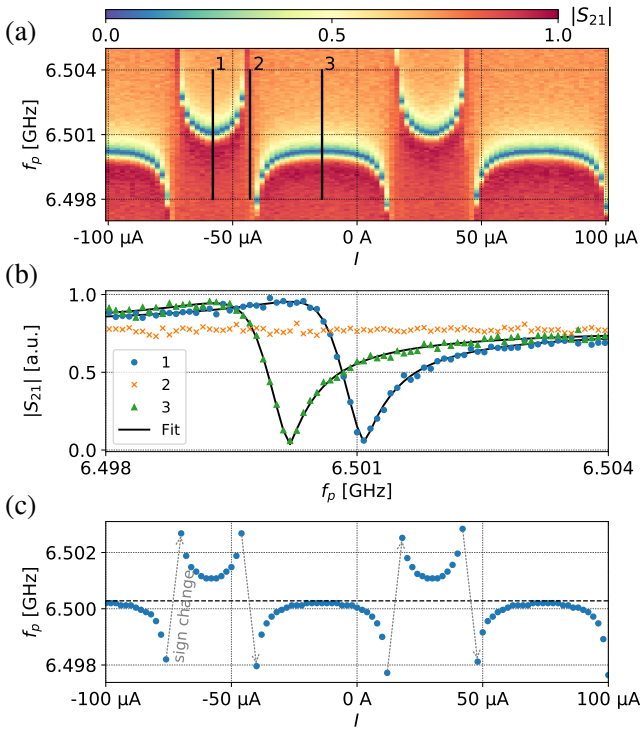

FIG. 2. (a) An experimental spectrum of a resonator strongly coupled to a transmon qubit depending on the coil current I. (b) Slices of the transmission from (a) showing two slices with fits (1,3) and a plateau with no dip (2) present. (c) Extracted data (blue dots) and mean frequency value over all points $\langle f_r \rangle_I$ (black dashed line). Grey arrows show where $f_r - \langle f_r \rangle_I$ changes sign.

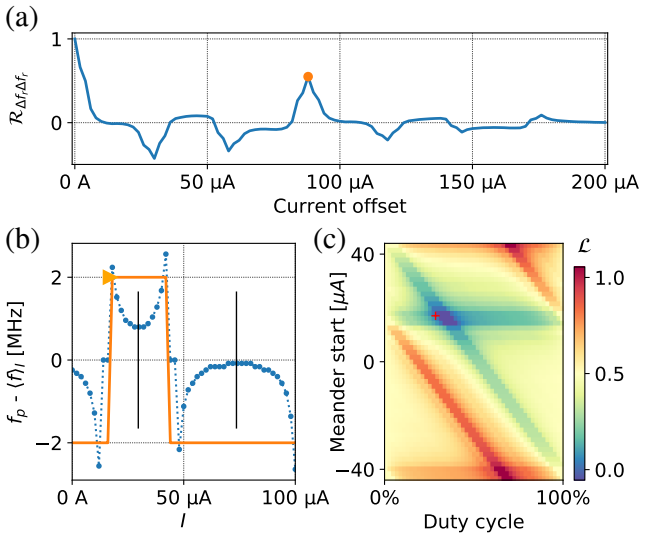

FIG. 3. Period and phase extraction procedure. (a) Autocorrelation function depending on the current offset ΔI shows a prominent local maximum at 88 μA (orange dot). (b) Construction for phase estimation; $\Delta f_r = f_r - \langle f_r \rangle_I$ (blue) is fitted with a square wave (orange, start marked with a triangle). Vertical bars mark candidate sweet spots. (c) Loss function (normalized) for the square wave fitting procedure from (b); red cross indicates the parameters of the meander shown there.

for each of them. Finally, we can polish the result in all six parameters using a local optimizer.

An outline of the method which uses Fig. 2(a) as an example is presented below. The chosen type of the resonator-qubit arrangement which yields the avoided crossings pattern is not universal: there are two other cases when the qubit spectrum lies entirely below or above the resonator frequency; however, they are treated exactly the same way and are simpler in terms of the loss function behaviour.

1. *Extracting $f_r(I)$ from data*

Firstly, we are going to reduce the dimensionality of the data, i.e. extract the resonance frequency for each I.

We do this by employing the *circlefit*[10] library which is capable of fitting various types of microwave resonators. For each I we fit the complex transmission $S_{21}(f_p)$ as in Fig. 2(b) (solid black lines) and extract the resonance frequency from the model. A possible caveat is that for some I values the resonance dip may disappear (see Fig. 2(b)) so the fit will fail. Therefore, such slices are excluded in advance via a threshold condition.

The resulting plot of the extracted resonator frequency versus current I is shown in Fig. 2(c) (blue dots). There are some current values located between the branches where the data points are missing, as expected, due to the absence of the resonance. Additionally, we plot here the mean value of the detected frequencies shown as a dashed black line. This parameter is important since it, will firstly, serve as an initial guess for the cavity frequency of the model (1): $f_c \approx \langle f_r \rangle_I$ and, secondly, will be used in the period and phase extraction algorithm which tracks the changes of the sign of the value $\Delta f_r = f_r - \langle f_r \rangle_I$ (marked as grey dashed lines in Fig. 2(c)). Locating these sign changes allows to find the qubit sweet spot without fittig the full model.

2. *Extracting period, phase and sweet spot locations*

As we have stated above, one of the serious obstacles for the fitting is the periodicity of the data on one of the fitting parameters. Along with the equally unknown phase of the signal, this leads to the presence of many local minima in the loss function which impede the progress of iterative optimization algorithms. In other words, the unknown parameters Π and I_{ss} are preventing us from finding the global minimum. Fortunately, it is possible to determine the period and the sweet spot location (or, the phase of the data) without fitting the full model (1) which alleviates the stated problem. In the absence of noise, this would be a trivial task. However, in the conditions of experiment, the noise to some extent is always present, so below we suggest a solution that is insensitive to local sporadic perturbations of the data.

A powerful tool for finding the period in a given dataset y

(especially when it contains just a few periods) is the autocorrelation function $\mathscr{R}_{yy}(l) = \sum_n y_n y_{n-l}$. The location of the largest of its local maxima (except for the $l = 0$) equals exactly the sought period. However, this is only true when the mean value of the function is zero; otherwise, $\mathscr{R}_{yy}(l)$ would be linear with a steep slope that may smear out all the extrema. Therefore, instead of directly calculating the autocorrelation of $f_r(I)$ we consider the function $\Delta f_r(I)$ introduced above which has zero mean and the same period. For this function, which looks exactly like one in Fig. 2(c) but centered vertically around zero, the autocorrelation function $\mathscr{R}_{\Delta f_r \Delta f_r}(\Delta I)$ depending on the current offset ΔI is shown in Fig. 3(a). As one can see, ΔI spans 200 μA just as the data itself. This means that to calculate $\mathscr{R}_{\Delta f_r \Delta f_r}(\Delta I)$ the data is being zero-padded at all ΔI except for $\Delta I = 0$, and this is why we get diminishing correlation peaks at Π, 2Π, etc. The orange dot in the plot shows the highest local extremum of $\mathscr{R}_{\Delta f_r \Delta f_r}(\Delta I)$ at 88 μA. It is a very prominent peak and can be easily distinguished among all others. There is as well a small peak at 176 μA which corresponds to $\Delta I = 2\Pi$. Note that the the autocorrelation function is not ideally smooth and has some abrupt bends on the sides of the peaks. This happens because there were some missing points in the data (corresponding to the plateaus of Fig. 2(b)) that were replaced by zeros to ensure the correct mapping between the current indices and current values. This zero padding may be noticed as well in Fig. 3(b).

Now, having found the period it is possible to precisely determine the phase of the signal. This is done via finding a global maximum of the zero-lag correlation function $\mathscr{R}_{\Delta f_r S}(0)$ between $\Delta f_r(I)$ and a square wave signal $S(I, \Pi, \phi, D)$ having the same period but unknown phase ϕ and duty cycle D. The high and low levels of the square must be opposite in value, i.e. 1 and -1, and the absolute value does not matter. An illustration of a square wave function satisfying the optimal condition is presented in Fig. 3(b) in orange. The phase ϕ (in μA) denotes the x-coordinate of the first point after the rising edge, and is marked with a triangle. Generally, the idea behind this is to robustly detect sign changes that were shown back in Fig. 2(c). We can not rely on a more simple algorithm that walks through the points and marks where the function changes its sign because such algorithm may fail in the presence of noise. Additionally, it will still work correctly even if the mean value $\langle f_r \rangle_I$ does not lie exactly between the branches and intersects one of them.

The global optimal ϕ and D are found using a brute force algorithm. It calculates the loss function $\mathscr{L} = -\mathscr{R}_{\Delta f_r S}(0)$ on a 50×50 grid of (ϕ, D) and takes the minimal value of all. This method is stable and universal due to the evident boundaries on $\phi \in [-\Pi/2, \Pi/2)$ and $D \in [0, 1]$. The loss function topography for the avoided crossing patterns is nicely structured and for our example is shown in Fig. 3(c). One peculiarity is that instead of a single minimum it has an area of the same minimal value. Again, this effect comes from the missing zero-padded f_r points at some I values. However, any value from this valley suits well enough for our purposes, and the algorithm finds no difficulty in locating it.

Having found values for Π, ϕ and D we now can calculate the currents of the transmon sweet spots in the case of the avoided crossings pattern and the smooth patterns:

$$I_{ss} = \begin{cases} \phi + \Pi(1+D)/2, \text{ for the avoided crossings} \\ \phi + \Pi D/2, \text{ otherwise} \end{cases} \tag{3}$$

To distinguish between these two cases when the noise is not too large, one may calculate the maximal absolute differential of the frequency data $\max_{i>0} |f_{r,i} - f_{r,i-1}|$ and compare it to the peak-to-peak amplitude $\max_{i,j} |f_{r,i} - f_{r,j}|$. For the avoided crossings these values are close and for the smooth dependencies they are not. However, in the presence of noise this indicator may fail, and one will have to check both current values to be I_{ss} by fitting the full model two times, and then choose among the two possibilities based on the loss value.

3. Full model fitting

Having performed the aforementioned preliminary steps, it is now possible to fit the full model to the extracted points. To do this, we employ brute force optimization combined with the Nelder-Mead simplex downhill algorithm[11] to polish the brute force result. For both methods, we use a common loss function defined as follows. For the known probe frequency span of the data Δf_p (Fig. 2(a), whole y-axis) and the set of N extracted points $\{p_i\} = \{(I_i, f_{r,i})\}$, we calculate the loss function as

$$\mathscr{L} = \frac{1}{N} \sum_{i=0}^{N} [f_{r,i} - \mathscr{M}(I_i,\, \Pi,\, I_{ss},\, f_c,\, g,\, f_{ge}^{max},\, d)]^2, \tag{4}$$

$$\mathscr{M} = \begin{cases} f_+, \ |f_+ - f_c| < \Delta f_p/2 \\ f_-, \text{ otherwise,} \end{cases} \tag{5}$$

where, as in the previous section,

$$f_\pm(I_i) = f_\pm(I_i,\, \Pi,\, I_{ss},\ \ f_c,\, g,\, f_{ge}^{max},\, d)$$

The condition of Eq. (5) means that we choose only the model frequencies that lie within a window Δf_p around the model f_c parameter. This ensures, firstly, that in the optimum we will not take any excess points outside the frequency scan, and, secondly, that we have a single model value for each current.

To substantiate the choice of the optimization algorithms, we present in Fig. 4 three visualizations of the the defined loss function. The plots show how the function behaves if a certain pair of 6 model parameters is varied while others are optimal. From the plots it is obvious that the loss function is ill-defined and has a lot of local minima. Moreover, it may not be smooth everywhere because of the condition (5). The f_{ge}^{max} and d parameters present the most significant difficulty in terms of false minima as can be seen from Fig. 4(a). In contrast, f_c presents the least difficulty, as can be seen from Fig. 4(b). The last plot Fig. 4(c) shows a very complex structure of the loss function and narrow optimal valleys and serves as an illustration of why the period and phase extraction algorithm is important.

The brute force algorithm acts on the grid specified in Table I. The ranges in the grid are based on the usual design parameters of the qubit samples in our database and the number

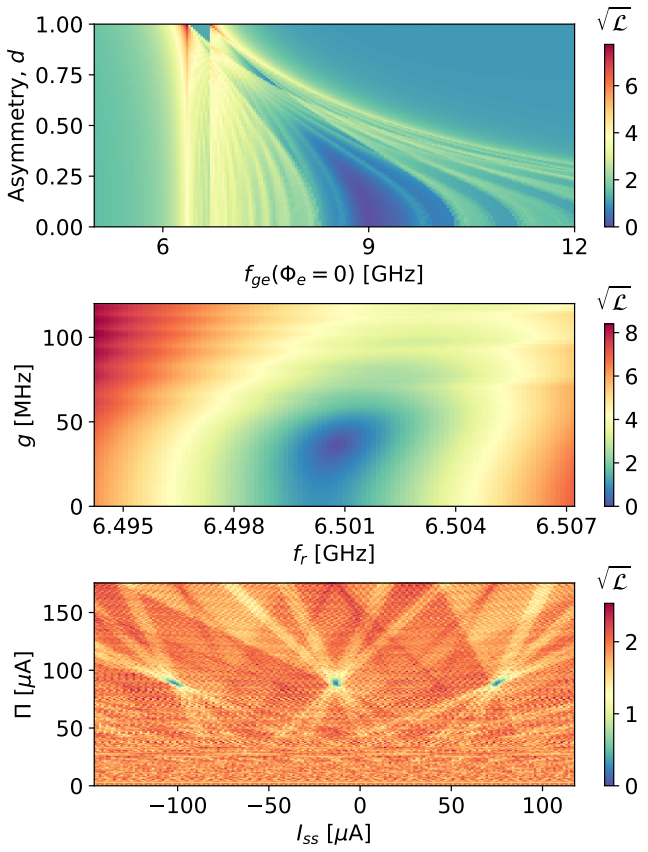

FIG. 4. Slices of the loss function (4) for the full model and experimental data from the example made around the optimal point. Root-mean-square per-point loss $\sqrt{\mathscr{L}}$ is in MHz. (a) f_{ge}^{max} and d are varied, other parameters optimal. A large valley is located near 9 GHz, and some smaller locally minimal ones are present all around. (b) g and f_r are varied, others optimal. The loss function for these two parameters is well-conditioned near the optimum. (c) Period $\Pi_{f_r} = \Phi_0/M$ and Φ_r/M varied, others optimal. This subplot illustrates a complex structure of local minima around the true one which we find analytically.

Parameter	Value range	Steps
f_c	$\langle f_r \rangle_I \pm 1$ MHz	3
g	20 - 40 MHz	5
f_{ge}^{max}	4 - 12 GHz	80
d	0 - 0.9	9

TABLE I. Grid specifications for the brute force algorithm for STS detection.

of steps is chosen so that the algorithm reliably finds the optimal valley. After the coarse brute force optimization is done and the optimal valley is located, we apply the Nelder-Mead search on all 6 parameters.

B. Two-tone spectroscopy recognition

Unfortunately, the resonator fitting procedure accuracy in terms of the qubit frequency (usually >50 MHz) is not enough in practical applications where it is necessary to obtain exact value of the qubit frequency down to 1-10 MHz. For the cQED systems, it may be done, in general, by trying to excite the qubit at different frequencies and then read it out expecting the e-state to be measured. The task is to find the exact location and shape of all the spectral lines depending on the magnetic flux that will be detected using such a method.

Particularly, in many groups the qubit spectrum is searched for using the so-called two-tone spectroscopy[12]. It is done by sending two microwave signals at the cQED system from which the first one, the probe tone, has a fixed frequency near f_c, and the frequency f_{exc} of the other, excitation tone, is varied. When the second signal becomes resonant with some transition (i.e., qubit ge transition), a shift of the cavity frequency occurs, and thus the transmission at the frequency of the first tone changes. This way, a heatmap showing the dependence of the frequency of various system transitions on the magnetic flux can be obtained.

An example from our database for a tunable transmon coupled to a notch-port resonator is displayed in Fig. 5. To obtain the two-tone spectrum in Fig. 5(b), for each current value the frequency of the first tone f_p is chosen to be equal to the frequency of the minimal transmission from the single-tone spectroscopy (STS), see Fig. 5(a). At the avoided crossing, this is not possible, and thus the frequency f_p may be chosen to be arbitrary within the scan area of the STS. This does not pose a problem since the two-tone spectroscopy is still only effective

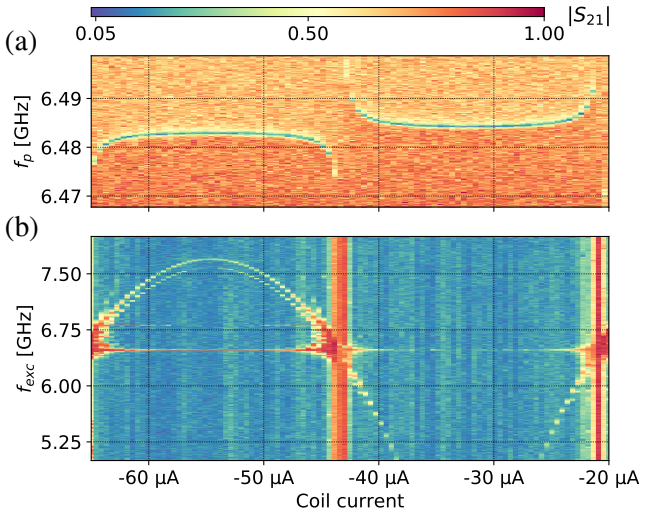

FIG. 5. Two types of spectroscopy results side by side; the colorbar is common, coil current scan range is the same. (a) Single-tone spectroscopy (one period on I). (b) Two-tone spectroscopy result. Clear flux-dependent transmon transitions are visible (ge and $gf/2$), and some fixed-frequency resonator excitations are present as well. Red vertical stripes are observed when the qubit and the cavity are close to resonance.

when the qubit and the resonator are detuned far from each other, i.e. in the dispersive regime[13], and would not work well near the resonant regime.

The resulting plot Fig. 5(b) shows the dependence of S_{21} on the magnetic flux and the excitation frequency. Most of the scan is in blue meaning that the resonator is not shifted and the probe tone gets almost entirely reflected (see colorbar). However, there are some different colour areas. Firstly, a bright and narrow horizontal line is observed near 6.5 GHz where the resonator is located. Likewise, there are two sharp horizontal lines just above 6.75 GHz which are from the crosstalk coupling to another on-chip resonator. Secondly, bright vertical stripes are seen at the current values corresponding to the avoided crossing areas. Finally, two transmon transitions of varying frequency are visible. The upper one is the *ge* transition, and the lower one is the two-photon $gf/2$ one; at each coil current, they are separated by $E_C/2h$, or half the anharmonicity of the transmon (see Table V).

The presence of several bright lines along with noise makes it in general impossible to accurately fit the data with the model (A3) using the standard curve fitting procedures. Additionally, when several multi-photon transitions are visible, it is hard for an algorithm to distinguish between them to find only the *ge* transition. This means that for robust qubit detection we need to fit all possible single- and multi-photon spectral lines simultaneously. Below, we present our approach to solve this problem.

1. Thresholding the data

Similar to the reasoning in section II A 1, the first thing to do is to reduce the three-dimensional picture Fig. 5 to two dimensions. This is done in several steps.

First, we calculate the median absolute transmission $\text{median}[S_{21}]_{f_{exc}}(I)$ for each current value (or frequency column). It gives us the background dependent only on I and not on f_{exc} which can be then subtracted from the data; then, the absolute value of the difference $Z = \left|S_{21} - \text{median}[S_{21}]_{f_{exc}}\right|$ may be plotted. The subtraction both removes the background and in each data column and highlights the points that are distinct in either amplitude or phase. For our example, the resulting image can be seen in Fig. 6. As one can notice, the background subtraction removes most of the vertical stripes that were present in Fig. 5(b).

Next, the data points may be extracted to form a 2D point array where the qubit lines may be searched for. This procedure is done in several steps. First of all, it is necessary to do thresholding of the data to obtain a binary image. We have tested various thresholding methods, i.e. Otsu's method[14]; however, the best performance in distinguishing local peaks from background was obtained using another method that is based on estimating the noise in the data. We estimate noise level σ by calculating the numerical difference between adjacent points in a row for each flux value, and then calculate the median absolute value:

$$\sigma = \text{median}\left[\left|Z_{i,j+1} - Z_{i,j}\right|\right]_{i,j},$$

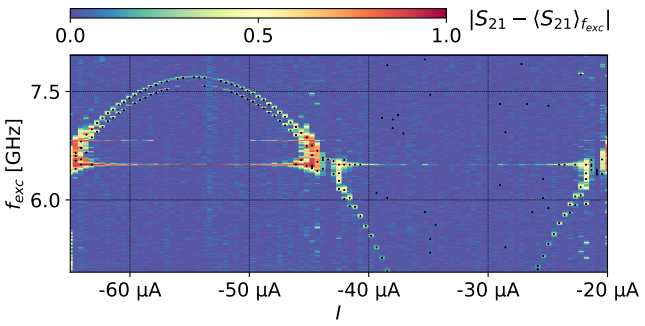

FIG. 6. Processed data and extracted and filtered datapoints (black crosses) that will be subject to fitting.

where i numerates current values, and j numerates excitation frequency values. Using median instead of mean reduces the impact of singular bright extrema that may be present in the row.

Next, for each row we use the *find_peaks* routine of the SciPy[15] library to detect all local extrema there, and then exclude those whose height is less than σ as probably originating from the noise.

After finishing the procedures above, we get an array of points that correspond to the most prominent peaks in the data. However, already at this point it is possible to remove all points that come from the fixed-frequency resonator spectral lines. This is done by excluding horizontal rows of points that have exactly the same frequency value within the resolution of the data.

The final extracted points are shown in Fig. 6 in black crosses. As one can see, the horizontal lines are correctly not included, and two qubit lines are almost fully represented. Background noise is mostly ignored, too.

2. Fitting binary data

a. General outline of the method. In most cases, even the filtered binary data contains noise and, importantly, is not single-valued for each flux value. This means that standard curve fitting methods are not applicable, and thus we resort to a hybrid algorithm that combines features of the Hough transform[16] for global optimization and Nelder-Mead search local optimization. The algorithm bases on three main parts: the point selection procedure, solution ranking and parameter sampling. The selection procedure is universal, and the latter two parts come in two variations depending on which type of optimization is used.

The general idea for the first part is illustrated in Fig. 7. Here, three narrow frequency bands of Δf are chosen around the model spectral lines calculated for tested parameters by (2). Points outside the bands are considered far away and are ignored. All the points inside a band are attributed to its line and included in its loss function. If at a certain flux there are several points inside a band, only the closest one is chosen and the rest (contentious) are ignored. Let $P_{1,2,3}$ be

the sets of points selected for corresponding transition lines $ge, gf/2, gd/3$ (in blue, orange and green in Fig. 7); the number of points in the sets are $N_{1,2,3}$, $N_\Sigma = \sum_i N_i$, and M is the total number of measured magnetic flux values. Finally, let $D_{1,2,3}$ be the corresponding sets of vertical distances between the selected points and the corresponding spectral lines.

The second part of the algorithm now has to evaluate the quality of the fit, i.e. be able to rank a supplied sets of optimization parameters. The ranking differs for the brute search and for the local optimization.

In case of the brute search, the evaluation is based both on the total number of selected points N_Σ and the normalized squared distances $\langle D_\Sigma^2 \rangle = \sum_i \sum_{P_i} D_i^2 / N_1$ (note that we normalize based just on N_1 to respect the majority voting in case of low N_2, N_3). Maximizing the total number of points included ought to have a higher priority than minimizing the average distances, since otherwise a single selected point lying exactly on the spectral line would win. However, in the presence of spurious spectral lines this prioritization may lead to wrong results since an incorrect solution with a slightly larger N_Σ but high normalized distance measure would overshadow the correct one with a low distance measure. To battle this effect and increase the influence of the distance loss, we quantize N_Σ into bins of size N_b equal to 25% of the total number of fluxes M, and then choose from the best bin the solution having the lowest distance measure.

Alternatively, for the Nelder-Mead algorithm one should build a loss function that returns just a single value instead of a double-valued rank as before. Since we still want to both maximize the number of points and minimize the mean distances, we take again same binned value $[N_\Sigma/N_b]N_b$ and $\langle D_\Sigma^2 \rangle$ but now calculate the function

$$\mathscr{L}_{N\text{-}M} = \frac{1}{[N_\Sigma/N_b]N_b} + \langle D_\Sigma^2 \rangle. \tag{6}$$

This loss function has a convex shape near the sought extremum; this makes it possible to run the Nelder-Mead algorithm without risk of escaping the optimal valley.

Finally, the third part of the algorithm is either the brute force search to find the global extremum or the Nelder-Mead descent to polish the found parameters.

Note the similarity between this construction and the Hough transform. The transform is implemented by quantizing the Hough parameter space into finite intervals or accumulator cells that each point votes for. Likewise, we use the frequency band (frequency quantization) to find the points voting for a certain parameter set; other parameters are as well quantized on a brute search grid. However, our approach is extended by a subsequent local optimization necessary since we want to improve the accuracy beyond brute grid resolution.

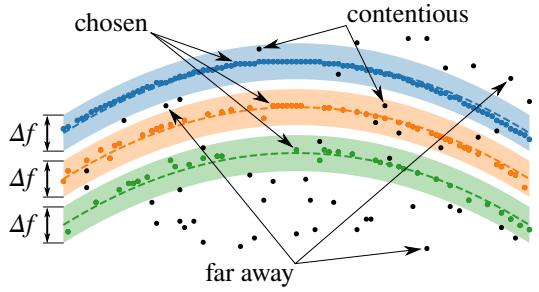

FIG. 7. An illustration for the loss function definition. In different colours are the frequency bands and the corresponding selected points, black points are ignored.

Optimization		I_{sws}	f_{ge}^{max}	d
Brute 1	range	$I_{ss}^{(0)} \pm .05\,\Pi^{(0)}$	$f_{ge}^{max,(0)} \pm 30\%$	0.1 - 0.9
Δf=100 MHz	steps	10	50	8
Brute 2	range	$I_{ss}^{(1)} \pm .02\,\Pi^{(0)}$	$f_{ge}^{max,(1)} \pm 100$ MHz	$d^{(1)} \pm 0.1$
Δf=50 MHz	steps	10	20	10

TABLE II. Grid specifications for the brute force algorithm in the single-line fitting. First iteration is a coarse search and the second is more accurate.

To sum up, the local optimization is done on points belonging to a narrow frequency band around the spectral line when this band contains as many points as possible. This logic is applicable both to single-line and multi-line fitting. In the following, we will use single-line fitting to find at least one spectral line in the point cloud, and then full multi-line fitting to detect all lines that may be present.

b. Single-line optimization First of all, we refine the given coarse initial values for the qubit parameters. We assume that the supplied period $\Pi^{(0)}$ is accurate which is true if the initial guess stems from the single-tone spectroscopy fitting, and that the other parameters may be inaccurate due to noise/magnetic flux shifts. So, only the sweet spot location $I_{ss}^{(0)}$, $f_{ge}^{max,(0)}$ and $d^{(0)}$ are optimized by brute force. The refinement is performed using a single spectral line by two brute force searches and then a Nelder-Mead optimization on the chosen points.

First brute force is done with a wide frequency band Δf=100 MHz around it and a grid specified in Table II. We do a rather wide search of 10% of the period Π around the initial sweet spot position $I_{ss}(0)$ since in our data there are sometimes inconsistencies between the single-tone and the two-tone spectroscopy that have been recorded on different days. In the real experiment, though, it is not usually necessary since flux drifts are rare if the two-tone scan is taken right after the single-tone. Due to rather large Δf value, the first search is used only to generally locate the extracted points in the parameter space. The found coarse optimum is denoted as $I_{ss}^{(1)}$, $f_{ge}^{max,(1)}$ and $d^{(1)}$.

Then, the second brute force is launched with contracted parameter ranges around the coarse optimum (see Table II) and reduced $\Delta f = 50$ MHz. This search already is aimed to locate the near-optimal point in the parameter space. Importantly, this step may not find exactly the highest line $f_{ge}(I)$, but it certainly will find one of the lines that has the most points in it, i.e. $f_{gf/2}(I)$, and thus get an incorrect value for $f_{ge}^{max,(2)}$. This behaviour can't be overcome except than by fitting multiple lines at the same time. For the other two parameters $I_{ss}^{(2)}$ and $d^{(2)}$ there is no ambiguity, and they are estimated accu-

Parameter	Value range	Steps #
f_{ge}^{max}	$f_{ge}^{max,(3)}{}^{+0.4\ \mathrm{GHz}}_{-0.0\ \mathrm{GHz}}$	10
α	0.2-0.3 GHz	10

TABLE III. Grid parameters for the multi-line brute search; $\Delta f = 50$ MHz for each line.

rately.

Finally, only the chosen points from the second brute force are used to fit the model using the Nelder-Mead algorithm which is allowed to polish not only the 3 resulting parameters from the second brute search but as well the period $\Pi^{(0)}$.

c. Multi-line optimization With the optimal parameters $I_{ss}^{(3)}$, $f_{ge}^{max,(3)}$, $d^{(3)}$ and $\Pi^{(1)}$ from the single-line fitting, we perform multi-line optimization. It as well consists of a brute search and the Nelder-Mead minimization. The loss function is defined the same way, but now three or four spectral lines should be taken into account.

This stage serves, firstly, to ensure the correct detection of the *ge* transition as the highest visible spectral line and, secondly, to find the anharmonicity α of the qubit. For transmons, all the lines have the same shape and differ only by a constant frequency shift (see Fig. 7). Since the single-line fitting procedure captures the shape of the line accurately, we only do the brute search upon the f_{ge}^{max} and α. The grid parameters may be found in Table III. We choose an asymmetric range for f_{ge}^{max} to ensure that the line comb in Fig. 7 moves only upwards from the single-line solution and finds the highest visible line if that one was not detected by the previous procedure. Anharmonicity is swept in a range that is typical for this type of qubits.

III. RESULTS

In this section, we discuss the performance and accuracy of the two algorithms described in the previous section. Firstly, we test the resonator spectrum recognition, and then the qubit spectrum detection algorithm.

A. Single-tone spectroscopy recognition

The algorithm was implemented in Python using the *brute* and *minimize* routines of the SciPy[15] library. We present here three examples of the detection for all possible qubit-resonator dispositions. The resulting fits are presented in Fig. 8 along with the original data and the error plots; we will further reference them as (a), (b) and (c).

The chosen algorithm order works as expected, as one can see from Table IV comparing the brute estimation and the final result after Nelder-Mead is performed. The significant improvement in the loss value of the polished result compared to the brute estimation is due to the more accurate determination of the cavity frequency f_c which leads as well to major shifts in optimal g, f_{ge}^{max} and d. However, even these optimal qubit parameters and coupling strength may be inaccurate even on GHz scale. For example, in case (b) for f_{ge}^{max} we see a 300 MHz difference between the optimal and the correct value found with TTS. For (a) and (c), the differences in f_{ge}^{max} are much smaller (about 10-70 MHz) but instead we see significant errors in d. Inaccuracy in the qubit parameters is caused by low sensitivity of the resonator frequency to the qubit frequency when they are far away and by

Finally, The match is almost perfect, and the noise in the residuals is random and thus shows no systematic errors. In Fig. 9 we also present the fitting results for different powers of added noise. The signal-to-noise ratio (SNR) is defined for our data in a similar manner as the SNR in the resonator fitting tests[10]; we take distance $2r$ between two maximally remote points of $S_{21}(f_p, I)$ among any pair on the complex plane (i.e., the diameter of the resonance circle) as the signal amplitude, and the noise of the form $\frac{\xi_1 + i\xi_2}{\sqrt{2}}$, where ξ_1, ξ_2 distributed normally with zero mean and variance (amplitude) σ. The SNR then is defined as r/σ. As one can see from the graph, the algorithm stays robust even at very low SNRs that are even lower than the low limit SNRs for the *circlefit* stability. This is possible because a fallback strategy of taking the smallest amplitude point as the resonance is applied when *circlefit* fails. Ultimately, the key point of this stress test is to show that the algorithm can be applied in real-life scenarios when the data may be of low quality.

The fitting example above runs for 3.2 seconds on a 5-year old Intel Core i5-3337U CPU, from which 2.7 seconds are for the brute and 0.4 of a second is for the Nelder-Mead minimization. On a contemporary Intel Core i7-7700 CPU, it takes about one second to run the whole procedure. The time costs mostly come from the square root calculation necessary for Eqs. (A3) and (B3) and because that the brute routine is not parallelized. However, this is still fast, firstly, because recording a resonator spectrum such as one in the example takes around 20 seconds, and, secondly, it is much faster than a human would do.

We have tested the algorithm on more than 100 real spectra that we have in our experimental database, and it finds an optimum for any kind of the dependence of the resonance on the flux caused by various dispositions of the qubit and the resonator, as in Fig. 12. Example fitting results for the variants in Fig. 12(b,c) are provided in **??**. There is a caveat, however, in some of such cases. It turns out, that for large qubit-

Parameter	(a)		(b)		(c)	
	Brute	N-M	Brute	N-M	Brute	N-M
f_c, GHz	6.5004	6.5007	6.962	6.9628	6.47	6.465
g, MHz	24	36.1	28	43.8	36	86.5
f_{ge}^{max}, GHz	8	8.97	9.2	9.38	6.3	5.89
d	0.5	0.09	0.6	0.61	0.1	0.325
Loss, kHz	251	24	313	39	2050	158

TABLE IV. Optimal parameters (rounded) found for the three cases in Fig. 8 after the brute and Nelder-Mead optimizations. The correct values for f_q^{max} and d (from TTS) are: (a) 9.04 GHz and 0.26; (b) 9.08 GHz and 0.6; (c) 5.9 GHz and 0.42.

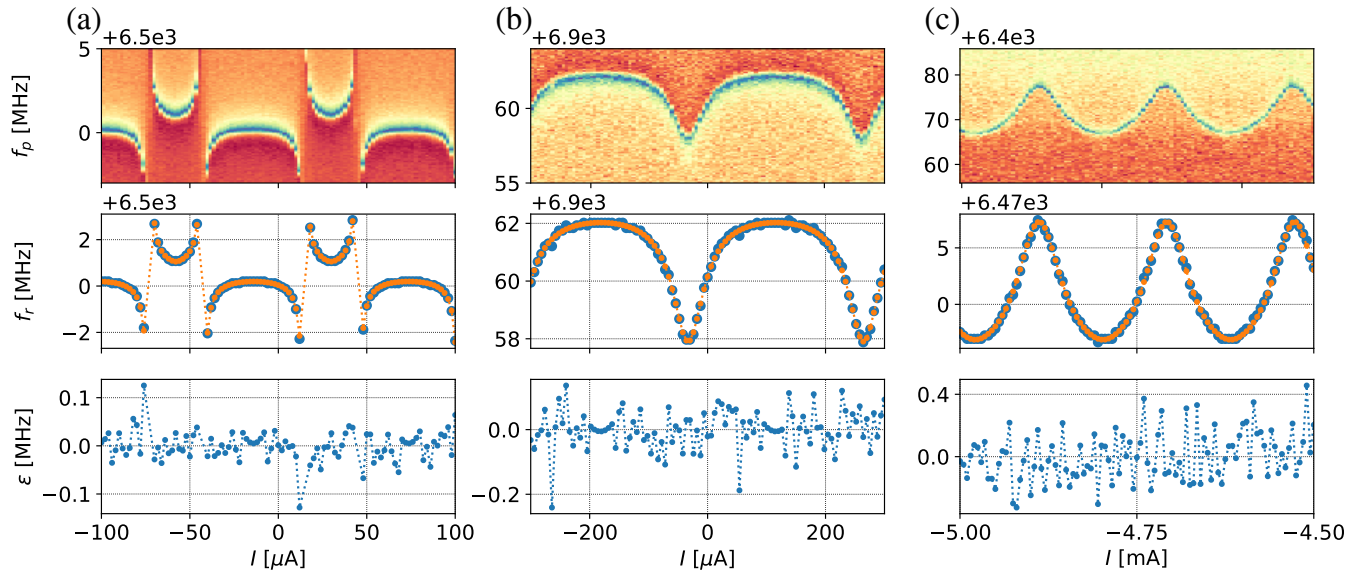

FIG. 8. The results of the algorithm execution on three experimental examples from our database. In the upper row, original images are presented. In the middle row, the data (blue dots) and the fitted model (orange connected dots) are shown. In the lower row are errors ε. (a) Avoided crossings pattern; per-point RMS error around 30 kHz. (b) The qubit entirely above the resonator; per-point RMS error around 60 kHz. (c) The qubit below the resonator; per-point RMS error around 150 kHz.

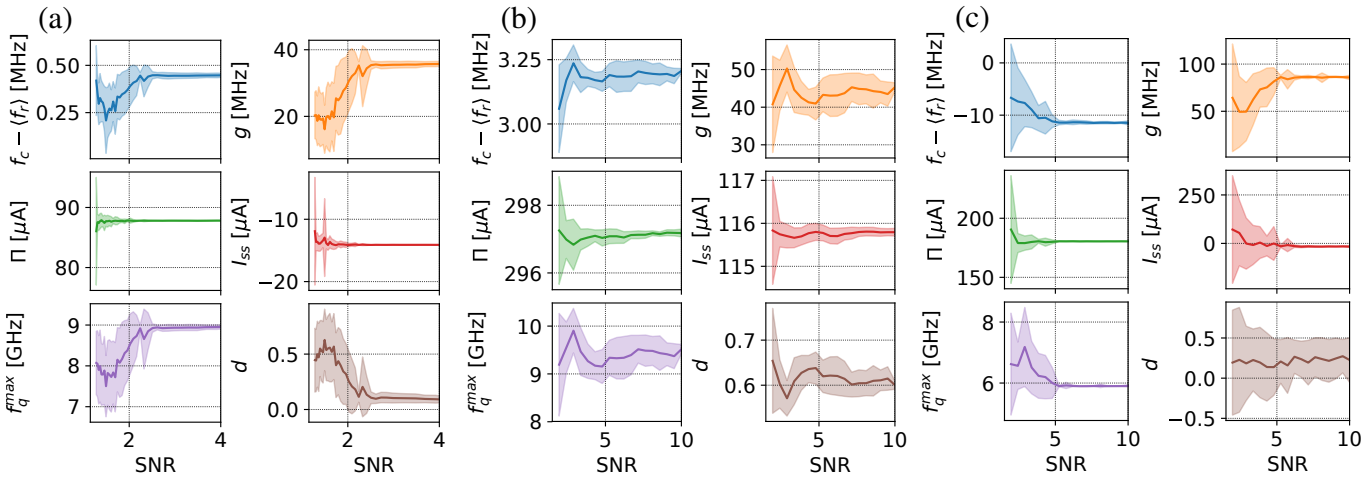

FIG. 9. Behaviour of the algorithm on the real data from Fig. 8 with added gaussian noise of varying power (i.e., with artificially reduced SNR). The clouds show standard deviations of optimal parameters after 50 tries, solid lines show mean values. (a) Detecting avoided crossings; the data used are from Fig. 8(a). The algorithm is accurate above SNR=3 but is still robust at detecting avoided crossings down to SNR=2 but with reduced accuracy in f_{ge}^{max}, g and d. (b) Detection for the case of smooth dependence of the resonator frequency on current; the data used are from Fig. 8(c). Due to the problems with the resonator fitting, the stability is reached only above SNR=5. Correct qubit parameters f_q^{max}=5.91 GHz and $d = 0.42$ (from TTS); f_q^{max} from the fit in the stable region is 5.89 GHz. However, d still can not be determined accurately on the data with noise;it is estimated to be 0.35 on the original data.

cavity detunings two different sets of parameters minimizing the loss function equally well are possible. An illustration for this statement can be seen in Fig. 10(a),(b). The algorithm was launched using different grid ranges for f_q^{max}. In one case (orange) the search was done below, and in the other (green) above the mean resonance frequency $\langle f_c \rangle_I$. The resulting fits are equally accurate, and without other information about the system it would not be possible to choose between the two. Therefore, some hints should be passed to the algorithm to avoid ambiguity; for instance, whether to look for the qubit above or below the resonator. Otherwise, it would be necessary to check both possibilities with other methods, i.e. via two-tone spectroscopy.

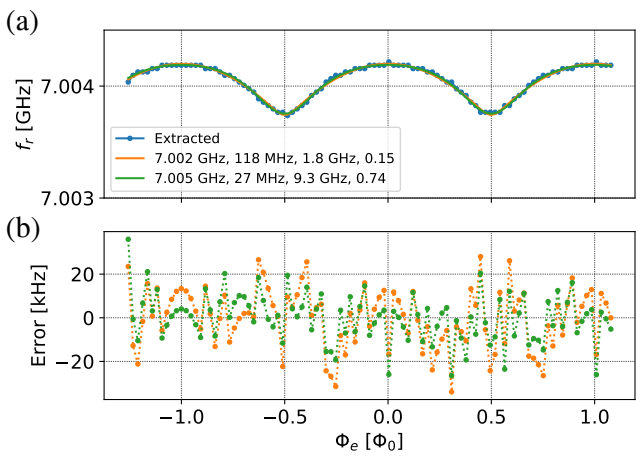

FIG. 10. (a) Two alternative fits (orange and green lines) for the same data (blue dots). The corresponding parameters f_c, g, f_{ge}^{max}, d for the two alternative fits are in shown the legend. (b) Residuals for the two fits, in orange (qubit below) and green (qubit above). RMS errors are 14 kHz and 11 kHz, respectively.

Level	Energy	Transition	Frequency
$g\ (E_0)$	0	ge	ω_{ge}
$e\ (E_1)$	$\sqrt{8E_JE_C}-E_C$	$gf/2$	$\omega_{ge}-0.5E_C$
$f\ (E_2)$	$2\sqrt{8E_JE_C}-3E_C$	$ef, gd/3$	$\omega_{ge}-E_C$
$d\ (E_3)$	$3\sqrt{8E_JE_C}-6E_C$	$ed/2$	$\omega_{ge}-1.5E_C$
E_4	$4\sqrt{8E_JE_C}-10E_C$	$fd, eE_4/3$	$\omega_{ge}-2E_C$

TABLE V. Energies and some transition (single and multi-photon) frequencies for the first 5 levels of the transmon calculated with (A3).

IV. DISCUSSION

Appendix A: Transmon Hamiltonian

The simplest version of this qubit consists of a Josephson junction shunted with a large capacitor. Flux tunability of the frequency is attained by replacing a single Josephson junction with a SQUID as in Fig. 11(a) and applying external magnetic flux Φ_e to its loop. This configuration can be equivalently represented with a shunted junction of tunable energy, Fig. 11(b). The Hamiltonian for such equivalent circuit is as follows:

$$\hat{H}_{tr} = 4E_C\hat{n}^2 - E_J(\Phi_e)\cos\hat{\varphi}, \tag{A1}$$

where $E_{J1,2}$ are the Josephson energies , $E_C = e^2/2C_\Sigma$, $C_\Sigma = C_s + C_1 + C_2$, is the charging energy, $\hat{n}$ and $\hat{\varphi}$ are the operators for the Cooper pair number and the phase of the qubit island. For the equivalent Josephson energy E_J one obtains

$$E_J(\Phi_e) = E_{J\Sigma}\cos(\pi\Phi_e/\Phi_0)\sqrt{1+d^2\tan^2(\pi\Phi_e/\Phi_0)}, \tag{A2}$$

where $E_{J\Sigma} = E_{J1} + E_{J2}$, $d = \frac{E_{J1}-E_{J2}}{E_{J1}+E_{J2}}$ is the asymmetry of the SQUID. As one can notice, the dependence is periodic in Φ_e.

It is also possible to derive analytical expressions for the energy levels and transition frequencies for this type of qubits.

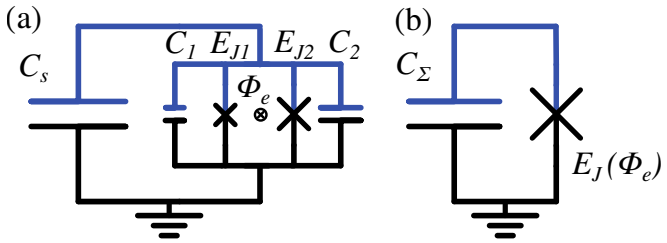

FIG. 11. (a) A tunable transmon circuit with an asymmetric SQUID, $E_{J1} \neq E_{J2}$. (b) Equivalent transmon with tunable energy $E_J(\Phi_e)$ and unified capacitance C_Σ. The qubit island containing its single degree of freedom is in blue.

The energy of the m^{th} level is[9]

$$E_m = m\sqrt{8E_J(\Phi_e)E_C} - \frac{E_C}{12}(6m^2+6m), \tag{A3}$$

and some of the transition frequencies are presented in Table V. The qubit frequency may be approximated as

$$\begin{aligned} f_{ge}(\Phi_e) &\approx \sqrt{8E_J(\Phi_e)E_C} \\ &= f_{ge}^{max}\sqrt{\cos(\pi\Phi_e/\Phi_0)\sqrt{1+d^2\tan^2(\pi\Phi_e/\Phi_0)}}, \end{aligned} \tag{A4}$$

where $f_{ge}^{max} = \sqrt{8E_J(0)E_C}$. This simplifies the expression for the frequency since now it depends on two parameters instead of three.

One final note is that in real-life applications is not possible to know directly the flux Φ_e that is threaded through the SQUID. The experimenter usually knows only the current I (or voltage) which he applies to some coil that is connected inductively to the SQUID. Then $\Phi_e = MI + \Phi_r$, where M stands for the mutual inductance of the coil and the SQUID, and Φ_r is some residual flux inherent to the sample.

Appendix B: Circuit QED

The readout of the superconducting qubits is now predominantly done using an ancilla system which is usually implemented as a superconducting microwave resonator which acts as an electromagnetic cavity in the standard cavity QED. Truncating the qubit to two levels, one may obtain the following Hamiltonian for the compound cavity-qubit system (in RWA):

$$\hat{H}/h = \frac{f_q}{2}\hat{\sigma}_z + f_c\hat{a}^\dagger\hat{a} + g(\hat{\sigma}^-\hat{a}^\dagger + \hat{\sigma}^+\hat{a}), \tag{B1}$$

where f_q is the qubit frequency, f_c is the cavity frequency and g is the coupling strength. As long as the RWA is done, this Hamiltonian may be diagonalized analytically[13]:

$$E_{g,0}/h = \frac{f_c - f_q}{2}, \tag{B2}$$

$$E_{\pm,n}/h = (n+1)f_c \pm \frac{1}{2}\sqrt{4g^2(n+1)+(f_q-f_c)^2}. \tag{B3}$$

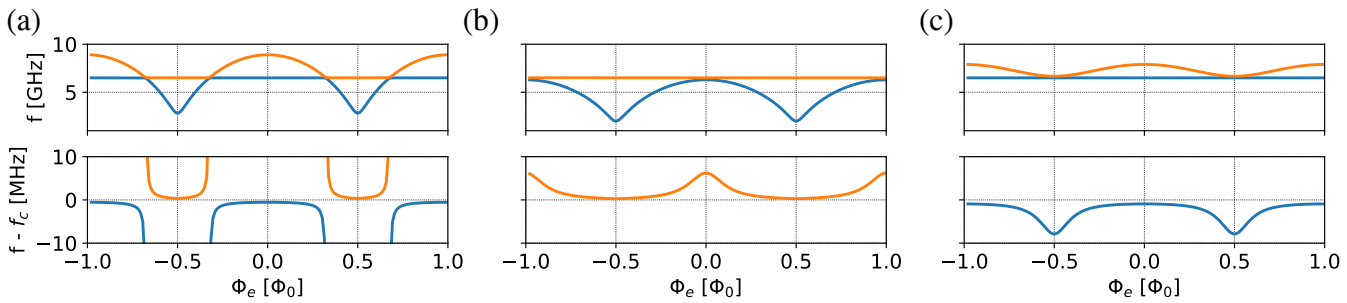

FIG. 12. Frequency spectrum of the transmon-resonator system. Parameters used: $f_{ge}(0) \approx \sqrt{8E_C E_J(0)}/2\pi = 8.5$ GHz, $d = 0.3$, $f_r = 6.4$ GHz, $g = 30$ MHz. For each subplot two transition branches $f_\pm = (E_{\pm,0} - E_{g,0})/2\pi$ are shown (orange and blue, respectively) both forming the resonator and qubit lines. As one can notice, there are three qualitatively different cases of the resonator-qubit disposition. Lower row shows a zoomed area around f_c that looks differently in each case.

This is very convenient for our purposes. By substituting the dependence of the qubit frequency $f_q \equiv f_{ge}(\Phi_e)$ into these equations, we can get straightforwardly the full system spectrum in dependence on the magnetic flux. In Fig. 12 we have used the equations (A3), (B2) and (B3) to model a tunable transmon interacting with a cavity for various Φ_e and various f_{ge}^{max}, d. In the lower row of the figure, one can see that it is possible to extract the dependence of the *cavity* frequency f_c on Φ_e; for example, the well-known avoided crossing pattern can be directly observed in Fig. 12(a), and the other two possible behaviours for the qubit entirely above or below the resonator in Fig. 12(b),(c). To shorten the notation, in the following we will define the corresponding branch frequencies of (B3) as $f_\pm = (E_{\pm,0} - E_{g,0})/2\pi$.

In Fig. 12(a) it is also possible to see the entire spectrum of a transmon *ge* transition predicted by equations (A2), (A3). It has a cosine-like periodic shape with a period of one flux quantum Φ_0. Consequently, it has two extrema, the upper and the lower which are called "sweet spots" due to the first-order insensitivity to Φ_e, and thus to possible flux noise. In the following, by saying sweet spot we will assume the upper one whose frequency is $f_{ge}(\Phi_e = 0) \equiv f_{ge}^{max}$.

We will use the model (B2), (B3) to fit the resonator frequency that we can find in an experiment. The only conceptual problem for the fitting that is left now is that the function we want to use as a model is not single-valued. Indeed, in Fig. 12(a, top) for each value of magnetic flux we always find two frequency points corresponding to the qubit and to the resonator, respectively. However, in practice only a narrow scan around the resonator frequency such as in Fig. 12(a, bottom) is required, and thus no ambiguity occurs.

[1] J. Kelly, P. O'Malley, M. Neeley, H. Neven, and J. M. Martinis, "Physical qubit calibration on a directed acyclic graph," arXiv preprint arXiv:1803.03226 (2018).
[2] S. M. Smith, *Metrology of Quantum Control and Measurement in Superconducting Qubits*, Ph.D. thesis, University of California Santa Barbara (2018).
[3] A. Blais, J. Gambetta, A. Wallraff, D. Schuster, S. Girvin, M. Devoret, and R. Schoelkopf, "Quantum-information processing with circuit quantum electrodynamics," Physical Review A **75**, 032329 (2007).
[4] D. A. Forsyth and J. Ponce, *Computer Vision: A Modern Approach* (Pearson, 2011).
[5] R. Versluis, S. Poletto, N. Khammassi, B. Tarasinski, N. Haider, D. Michalak, A. Bruno, K. Bertels, and L. DiCarlo, "Scalable quantum circuit and control for a superconducting surface code," Physical Review Applied **8**, 034021 (2017).
[6] J. Kelly, R. Barends, A. G. Fowler, A. Megrant, E. Jeffrey, T. C. White, D. Sank, J. Y. Mutus, B. Campbell, Y. Chen, *et al.*, "State preservation by repetitive error detection in a superconducting quantum circuit," Nature **519**, 66 (2015).
[7] M. Jerger, *Experiments on superconducting qubits coupled to resonators*, Ph.D. thesis, Karlsruhe Institute of Technology (2013).
[8] B. J. Bloom, S. A. Caldwell, M. Reagor, and C. Rigetti, U.S. Patent No. US 20180260732A (13 Sep. 2018).
[9] J. Koch, M. Y. Terri, J. Gambetta, A. A. Houck, D. Schuster, J. Majer, A. Blais, M. H. Devoret, S. M. Girvin, and R. J. Schoelkopf, "Charge-insensitive qubit design derived from the cooper pair box," Physical Review A **76**, 042319 (2007).
[10] S. Probst, F. Song, P. Bushev, A. Ustinov, and M. Weides, "Efficient and robust analysis of complex scattering data under noise in microwave resonators," Review of Scientific Instruments **86**, 024706 (2015).
[11] J. A. Nelder and R. Mead, "A simplex method for function minimization," The computer journal **7**, 308–313 (1965).
[12] A. Wallraff, D. Schuster, A. Blais, J. Gambetta, J. Schreier, L. Frunzio, M. Devoret, S. Girvin, and R. Schoelkopf, "Sideband transitions and two-tone spectroscopy of a superconducting qubit strongly coupled to an on-chip cavity," Physical Review Letters **99**, 050501 (2007).
[13] A. Blais, R.-S. Huang, A. Wallraff, S. M. Girvin, and R. J. Schoelkopf, "Cavity quantum electrodynamics for superconducting electrical circuits: An architecture for quantum computation," Physical Review A **69**, 062320 (2004).
[14] N. Otsu, "A threshold selection method from gray-level histograms," IEEE transactions on systems, man, and cybernetics **9**, 62–66 (1979).
[15] E. Jones, T. Oliphant, P. Peterson, *et al.*, "SciPy: Open source scientific tools for Python," (2001–), [Online; accessed <today>].
[16] P. V. Hough, "Method and means for recognizing complex patterns," (1962), uS Patent 3,069,654.